PAPER

Sn– and SnO2–graphene flexible foams suitable as binder-free anodes for lithium ion batteries

Cristina Botas,[a] Daniel Carriazo,*[ab] Gurpreet Singh[a] and Teófilo Rojo[ac]

With the objective of developing new advanced composite materials that can be used as anodes for lithium ion batteries (LIBs), herein we describe the synthesis of novel three dimensional (3D) macroporous foams formed by reduced graphene oxide (rGO) and submicron tin-based particles. The aerogels were obtained by freeze/freeze-drying a suspension of graphene oxide (GO) in the presence of a tin precursor and its subsequent thermal reduction under an argon atmosphere. The materials exhibited a 3D-macroporous structure formed by the walls of rGO decorated with Sn or SnO_2 particles depending on the temperature of calcination. Self-standing compressed foams were directly assembled into coin cells without using any metallic support to be evaluated as binder-free anodes for LIBs. The homogeneous dispersion and intimate contact between the Sn-based particles and graphene walls were confirmed by scanning electron microscopy (SEM). The performance of SnO_2–rGO composite materials as anodes for LIBs showed higher specific capacity compared with rGO and metallic Sn-containing samples, reaching a reversible capacity of 1010 mA h g^{-1} per mass of the electrode at 0.05 A g^{-1} and good capacity retention (470 mA h g^{-1}) even at 2 A g^{-1} ($\sim$2 C), among the highest reported for similar systems. The SEM images of selected electrodes after 50 charge–discharge cycles showed that even though SnO_2 submicron particles were pulverized into small nanoparticles they remain intact upon cycling.

Introduction

Lithium ion batteries (LIBs) are the dominant energy storage devices in portable electronic devices because of their high energy density and low self-discharge rate.[1] However, the increasing complexity of portable electronic devices and the envisioned development of flexible electronic devices, such as wearable electronic devices or roll-up displays, require the development of flexible and lightweight materials suitable to be used as electrodes that can store as much energy as possible, and could be charged as fast as possible.[2,3]

Graphite, with a theoretical gravimetric capacity estimated at 372 mA h g^{-1}, is to date the most commonly used material as anodes in LIBs because of its abundance, good electrical conductivity and low cost. With the aim of improving the energy, power and stability of LIBs, new materials have been proposed to replace graphite as anodes. Sn or SnO_2 with theoretical reversible specific capacities of 994 and 782 mA h g^{-1},[4,5] respectively, is among the most promising compounds that have been pointed out as alternative anode materials. The main drawback associated with the performance of Sn or SnO_2 as active materials for LIBs is its volume change (up to 300%) that occurs upon the lithiation/delithiation process. This extreme increase in SnO_2 volume can cause the pulverization of the material and/or the growth of an unstable solid electrolyte interface (SEI), which generally leads to low coulombic efficiencies and capacity fading along the cycling process.[6]

To overcome this drawback, different strategies such as the use of novel binders or the encapsulation of Sn-based particles have been proposed.[7–10] Graphene, an allotrope of carbon consisting of a monolayer of carbon atoms,[11] with outstanding properties such as flexibility and transparency, electrical conductivity or high specific surface areas, is used as a promising material to wrap up or to imbibe Sn-based particles.[12] It has been claimed that the presence of graphene not only improves the electronic conductivity of the composites, and therefore their capacity retention at high current rates, but also, graphene sheets can buffer the volume changes undergone by Sn-based particles.[13] Different approaches such as physical mixing of SnO_2 nanoparticles together with graphene sheets[14] or spray deposition[15,16] have been described for the preparation of these graphene–SnO_2 composites. However, the most explored strategy involves the hydro- or solvo-thermal deposition of very small SnO_2 nanoparticles (generally around 5 nm) on GO layers,[17–20] and their subsequent partial reduction by thermal treatments at moderate temperatures under an inert atmosphere[21,22] or through their reaction with hydrazine.[23,24]

On the other hand, graphene macroporous 3D foams showing interesting features, namely excellent mechanical strength and high specific surface areas, have been recently

[a]CIC EnergiGUNE, Parque Tecnológico de Álava, Albert Einstein 48, 01510 Miñano, Álava, Spain. E-mail: dcarriazo@cicenergigune.com

[b]IKERBASQUE, Basque Foundation for Science, Bilbao, Spain

[c]Departamento de Química Inorgánica, Universidad Del País Vasco UPV/EHU, 48080 Bilbao, Spain

evaluated as catalysts, adsorbents or as electrodes for super-capacitors[25] or LIBs.[26,27] However, to the best of our knowledge, SnO_2–graphene foams as anodes for LIBs have been scarcely explored.[22,24,28]

Recently, Feng *et al.* reported the preparation of SnO_2–graphene by hydrothermal treatment and subsequent chemical reduction with hydrazine, showing a capacity value of 661 mA h g^{-1} at 0.5 A g^{-1} after 60 cycles.[24] In a posterior study,[22] the authors tailored the macroporosity of these composites using polymeric templates to obtain highly macroporous scaffolds that were thermally reduced at 450 °C, claiming in this later case a specific capacity of 900 mA h g^{-1} at 0.4 A g^{-1}. In all these studies, very small SnO_2 nanoparticles (5 nm) on graphene sheets were reported and the materials were ground to powder to be further processed with conductive carbon in order to improve their electrical conductivity, and a binder (PVDF) for their evaluation as anodes in LIBs.

Herein we present the preparation of flexible macroporous 3D composites formed by reduced graphene oxide and submi-cron Sn or SnO_2 particles by a very simple route, which involves freeze/freeze-drying a suspension of graphene oxide in the presence of a tin precursor and subsequent thermal treatment (650 or 800 °C). The resultant materials were evaluated as self-standing binder-free anodes for LIBs, showing, in the case of the composites formed by SnO_2, very good stability after 400 charge–discharge cycles and reversible capacities per mass of the electrode of 1010 and 470 mA h g^{-1}, measured at 50 mA g^{-1} and 2 A g^{-1}, respectively. Some of the samples were additionally characterized after 50 charge–discharge cycles to obtain insight into the possible deactivation process observed for the sample calcined at 800 °C.

Experimental section

Synthesis of reduced graphene oxide aerogels and Sn-based composites

A GO suspension (2 mg mL^{-1}) was prepared according to a procedure previously described elsewhere.[29] In the first step, graphite oxide was obtained from synthetic graphite provided by Timcal (TIMREX-SFG75) by a modified Hummers method. This method makes use of the Hummers reagents with additional amounts of $NaNO_3$ and $KMnO_4$. Briefly, 360 mL of concentrated H_2SO_4 solution was added into a mixture formed by 7.5 g of synthetic graphite and 7.5 g of $NaNO_3$. The mixture was then cooled down using an ice bath. Once the mixture was cooled down, 45 g of $KMnO_4$ was slowly added in small doses to maintain the reaction temperature below 20 °C. The solution was then heated up to 35 °C and stirred for 3 h. After this period, 1.5 L of H_2O_2 (3% in weight) solution was slowly added, giving rise to a pronounced exothermal effect that increased the temperature up to 98 °C, and the reaction mixture was further stirred for 1 h. The remaining solid material was washed with different amounts of water and centrifuged again. A GO suspension of (2 mg mL^{-1}) was obtained by sonicating a diluted suspension of graphite oxide for 1 h, and then the suspension was centrifuged (3500 rpm, 30 min), after which any remaining solid was discarded.

For the preparation of the GO aerogels, 100 mL of the graphene oxide suspension (1 mg mL^{-1}) was suddenly frozen in liquid nitrogen and then freeze-dried in a Telstar LyoQuest freeze drier. GO monoliths were then calcined at 650 °C for 1 h under an argon atmosphere to obtain reduced graphene oxide samples (hereafter denoted as rGO). Tin containing samples were synthesized by dissolving 100 mg of $SnSO_4$ in 100 mL of the GO suspension (1 mg mL^{-1}), and then the pH was increased to 9 by the addition of some drops of a 1 M NH_3 solution. The mixture was heated at 60 °C for 5 h, and the suspension was then freeze/freeze dried to obtain macroporous Sn–graphene oxide composites. Sn–reduced graphene oxide aerogels were obtained by the pyrolysis of the aerogels in a horizontal tube furnace. Samples were heated at 1 °C min^{-1} to 200 °C to avoid the thermal blasting of GO and then to 650 or 800 °C at 2 °C min^{-1} under a dynamic argon atmosphere (100 mL min^{-1}), and maintained at this temperature for 1 h. These samples are hereafter denoted as Sn–rGO-650 and Sn–rGO-800.

Characterization

X-ray diffraction (XRD) patterns were recorded for powdered samples in a Bruker D8 X-ray diffractometer; data were collected at 40 kV and 30 mA using CuKα radiation over 2θ within the range of 20 to 70° at steps of 0.02° and a residence time of 5 seconds. Raman spectra were recorded with a Renishaw spectrometer (Nanonics multiview 2000) operating at an excitation wave-length of 532 nm. The spectra were acquired after 10 seconds of exposition time of the laser beam to the sample. Scanning electron microscopy (SEM) images were acquired with a field emission Quanta 200 FEG microscope from FEI. X-ray photoelectron spectroscopy (XPS) measurements were carried out in a UHV spectrometer chamber with base pressure below 10^{-10} mbar. The chamber features a hemispherical analyser PHOIBOS 150 with a 2D-DLD detector (SPECS) and mono-chromated X-ray source FOCUS 500 (SPECS) with two anodes: Al Kα ($h\nu = 1486.74$ eV) and Ag Lα ($h\nu = 2984.3$ eV).

Electrode assembly and electrochemical characterization

Electrochemical measurements were carried out in CR2032 type coin cells assembled inside a glove box under an argon atmosphere. Half cells were fabricated with the following configuration: Li/separator/rGO samples. Self-standing pellets of 12 mm in diameter and approximately 0.07 mm in thickness, showing densities between 0.10 and 0.15 g cm^{-3}, were obtained by punching out a compressed piece of our monolithic material and used as binder-free working electrodes; lithium metal foil was used as counter/reference and 1.2 M LiPF$_6$ in ethylene carbonate and dimethyl carbonate 1 : 1 (v/v) was used as the electrolyte.

Cyclic voltammetry (CV) curves were recorded in a multi-channel potentiostat/galvanostat (Biologic VMP3) at a scan rate of 0.1 mV s^{-1}. Electrochemical impedance spectroscopy (EIS) measurements were also carried out in a Biologic VMP3 station within the 100 kHz to 10 mHz frequency range.

This journal is © The Royal Society of Chemistry 2015

J. Mater. Chem. A, 2015, **3**, 13402–13410 | **13403**

Galvanostatic charge and discharge tests were run in a MACCOR battery tester at different current rates and the specific capacities were calculated per mass of the electrode.

Results and discussion

To obtain homogeneous composites formed by GO and tin-based particles, tin sulphate was dissolved in a suspension of GO (1 mg mL^{-1}) in water and the mixture was stirred for 24 h. Just a few minutes after the addition of the tin precursor, the GO suspension turned from brownish yellow to black, indicating that a partial reduction of the GO sheets had taken place or a certain agglomeration occurred, but at this point no precipitate was detected. Then, pH was increased by the addition of some drops of a 1 M ammonia solution to induce the homogeneous precipitation of the tin precursor on the GO layers and to prevent further agglomeration of the graphene sheets.[30] To assemble the GO sheets and Sn-based particles into a macroscopic macroporous 3D monolithic foam, suspensions were first freeze/freeze dried, and then heated under an argon atmosphere at 650 or 800 °C to remove part of the functional groups initially present on the GO layers and partially reduce them.

Photographs of GO–tin precursor and Sn–rGO-650 foams, obtained after the thermal reduction of the former one at 650 °C (Fig. 1A and B), show the macroscopic view of these self-standing monolithic structures, for which integrity is preserved even after being subjected to thermal reduction treatments. Together with them, other photographs of a film (Fig. 1C) and two electrodes of 12 mm in diameter (Fig. 1D) obtained by physically pressing the Sn–rGO-650 sample evidence the flexible nature of these self-standing films. Fig. 1 also includes the SEM images of the three samples (rGO, Sn–rGO-650 and Sn–rGO-800) recorded at different magnifications. SEM images of the rGO aerogel (Fig. 1E and F) show a disordered highly opened macroporous structure formed by thin sheets of rGO. This characteristic macroporous microstructure is produced as a consequence of the sublimation of the ice crystals, which are randomly formed by the fast freezing of the suspension in liquid nitrogen. The freeze-drying process did not only allow the formation of these low dense porous 3D structures, but it also helped to avoid the re-stacking of the layers within the materials. SEM images obtained for the sample Sn–rGO-650 (Fig. 1G and H) show, in addition to the microstructured rGO layers, the presence of highly homogeneous distribution of particles of approximately 250 nm in diameter attached to or embedded within the graphene sheets.

The sample obtained after calcination at 800 °C (Sn–rGO-800) (I and J images of Fig. 1) still exhibits a highly opened macroporous structure formed by rGO sheets together with Sn-based spherical particles. It is worth noting that increasing the calcination temperature from 650 to 800 °C gave rise to a significant increase in the size of the Sn-based particles, reaching values of 700 nm in diameter in the case of Sn–rGO-800. The element compositions obtained from the EDX analysis performed on these samples are summarized in Table 1. In both Sn-containing aerogels, the amounts of tin were quite similar
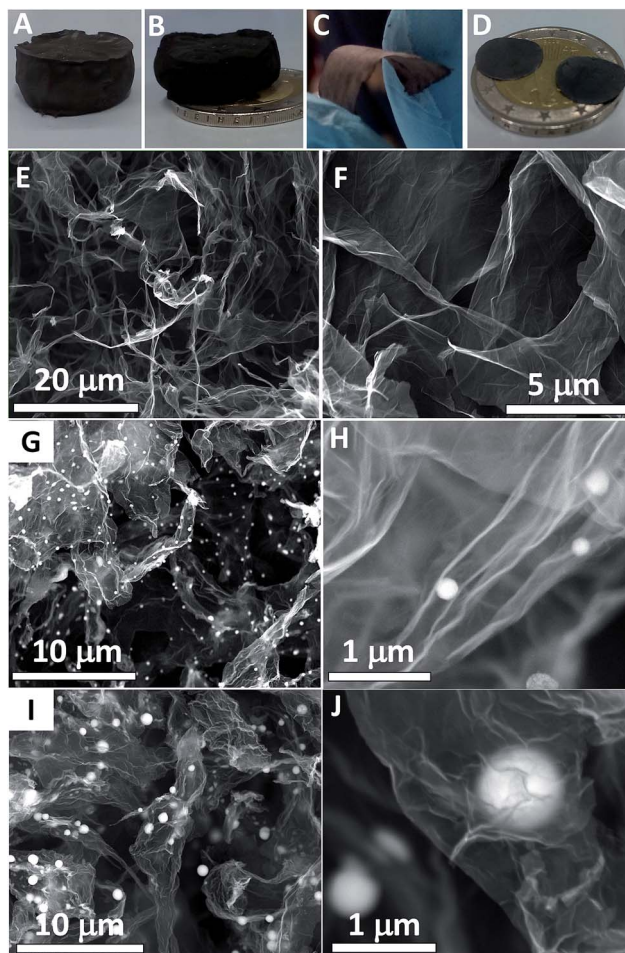

Fig. 1 Digital photographs of an aerogel obtained by freeze/freeze drying a 1 mg mL^{-1} suspension of graphene oxide in the presence of the Sn precursor (A), a monolithic Sn–rGO-650 sample (B), a bended film obtained upon pressing the Sn–rGO-650 aerogel (C) and two electrodes of 12 mm in diameter of sample Sn–rGO-650 on top of a 2€ coin (D). SEM images of the rGO aerogel (E and F), Sn–rGO-650 (G and H) and Sn–rGO-800 (I and J) samples.

Table 1 Summary of the thermal treatment conditions, composition and crystalline phases of the prepared samples

	Temperature (°C)	C^a (wt%)	O^a (wt%)	Sn^a (wt%)	Crystalline phase^b	I$_D$/I$_G$^{c}
rGO	650	91.9	7.7	—	rGO	0.9
Sn–rGO-650	650	55.6	8.8	35.8	SnO$_2$	1.1
Sn–rGO-800	800	58.0	3.5	38.5	Sn	1.1

^{a} Values measured by EDX analysis. ^{b} Major crystalline phase determined by XRD. ^{c} I$_D$/I$_G$ ratios measured from Raman spectroscopy.

and represent approximately 37% in weight of the mass of the composite. The main difference found between the sample calcined at 650 °C and the sample calcined at 800 °C is the lower oxygen content (3.5% wt for the Sn–rGO-800 and 8.8% wt for the Sn–rGO-650), which can be attributed to a further reduction of the tin oxide particles and the functional groups still present on the GO sheets at the higher temperature.

The XRD patterns obtained for the rGO aerogels, together with those obtained for the samples Sn–rGO-650 and Sn–rGO-800 are shown in Fig. 2. The diffractogram obtained for the rGO aerogel only shows a diffraction peak centered at 26.1° characteristic of the (002) planes of rGO. This broad diffraction indicates a poor ordering of the sheets along the stacking direction, pointing out that the sample comprised only a few graphene layers. The XRD pattern obtained for the sample Sn–rGO-650 (Fig. 2) also shows three major peaks at 26.5°, 33.8° and 51.7° assigned to the (110), (101) and (211) planes of the SnO_2 (JCPDS card 41-1445) together with other very low intense peaks recorded at 30.5, 32.0, 43.9 and 44.9° assigned to metallic tin in a tetragonal phase (JCPDS card 04-0673). It has been previously reported that the complete carbothermal reduction of SnO_2 to metallic tin takes place at 600 °C or even at lower temperature under an reductive atmosphere,[31,32] however, it seems that in our particular case the functional groups, together with the counterions present on the surface of the graphene sheet, could slightly increase the temperature of this process maintaining SnO_2 as the predominant species within this sample. The XRD pattern recorded for the sample calcined at 800 °C (Sn–rGO-800), also plotted in Fig. 2, clearly shows very sharp and intense peaks at 30.6, 32.1, 43.8 and 45.0°, all of them ascribed to metallic Sn in a tetragonal phase (JCPDS card 04-0673).

The Raman spectra (Fig. 2) recorded for the three samples (rGO, Sn–rGO-650 and Sn–rGO-800) show bands at 1350 and 1580 cm^{-1}, which correspond to the disordered (D) and graphitic (G) bands of carbon materials, respectively. The spectra recorded for the tin-containing samples exhibit an increase in the D/G intensity ratio with respect to the rGO sample (Table 1), which could be ascribed to a decrease in the average size of the sp^2 domains and an increase in the number of those domains probably due to the reaction between the Sn precursor and the graphene layers. Two low intense bands at 460 and 620 cm^{-1} were also detected in the Raman spectrum of the sample Sn–rGO-650, which can be assigned to the E_g and A_{1g} active modes of crystalline SnO_2 (inset of Fig. 2).[33]

The XPS spectra recorded for all these samples (Fig. 3) confirmed the presence of tin species within the Sn–rGO-650
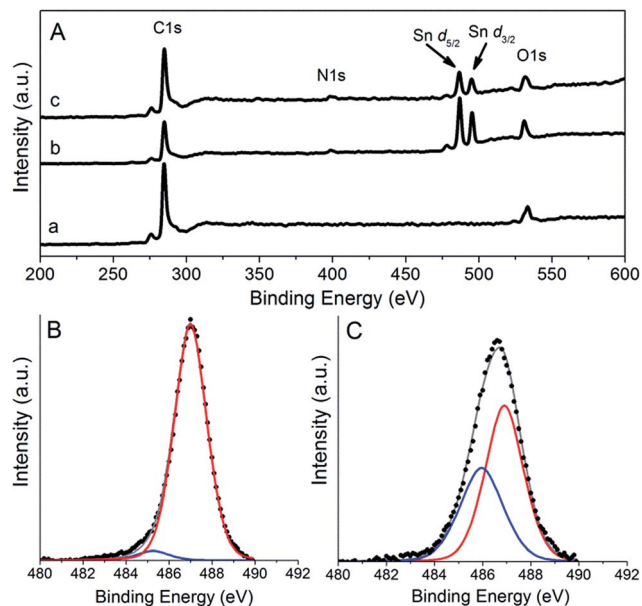

Fig. 3 XPS spectra (A) recorded for samples rGO (a), Sn–rGO-650 (b) and Sn–rGO-800 (c) and deconvoluted Sn d5/2 peaks recorded for Sn–rGO-650 (B) and Sn–rGO-800 (C) samples. Blue line (Sn^0) and red line (Sn^{4+}).

and Sn–rGO-800 samples. The XPS results also supported the fact that the major species present in the Sn–rGO-650 sample is Sn^{4+} and only a small fraction could be attributed to metallic Sn. In the case of the Sn–rGO-800 sample, the percentage of metallic Sn was significantly higher compared to the sample Sn–rGO-650 (Fig. 3). It is worth mentioning that a certain amount of Sn^{4+} was also identified in the sample Sn–rGO-800, which was not detected by XRD. In this case, the presence of Sn^{4+} should be ascribed to a partial oxidation of the tin surface when the sample was exposed to air. The Sn^{4+} amount was easily detected due to the surface-sensitive nature of the XPS technique. The XPS spectra recorded for both Sn-containing samples also showed low intense peaks centered at 398.8 eV, which are attributed to the presence of nitrogen incorporated
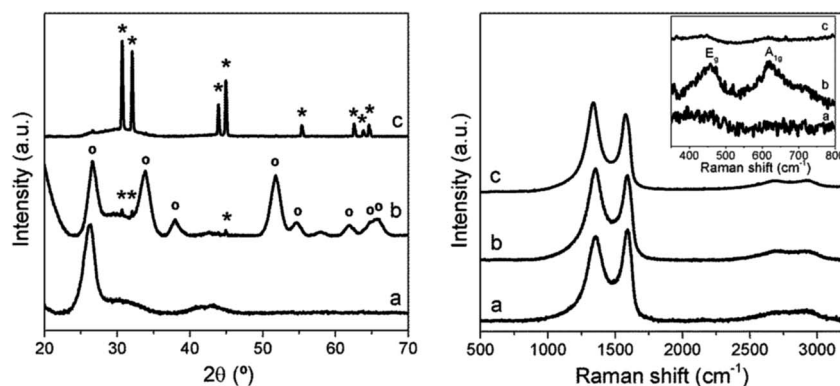

Fig. 2 XRD patterns (left figure) and Raman spectra (right figure) recorded for samples rGO (a), Sn–rGO-650 (b) and Sn–rGO-800 (c). Peaks assigned to tetragonal metallic Sn and SnO_2 cassiterite phases are marked with (*) and (°), respectively. The inset shows the enlarged region between 350 and 800 cm^{-1} of the corresponding Raman spectra.

during the synthesis process. The XPS spectrum recorded for the pristine aerogel (rGO) showing only peaks assigned to C 1s and O 1s is also included in Fig. 3 for comparison.

The electrochemical behaviour of tin-containing materials as anodes was first evaluated by cyclic voltammetry (CV). The electrodes were prepared, as described above, by pressing and punching out self-standing binder-free electrodes with 12 mm in diameter and approximately 0.07 mm in thickness, namely densities between 0.1 and 0.15 g cm^{-3}. These values are higher compared with those of graphene-based aerogels but still lower than those of graphite anodes usually obtained at the lab scale, which ranged 1.3 g cm^{-3}, approximately. Fig. 4 shows the first four CV curves recorded for the Sn–rGO-650 and Sn–rGO-800 samples in the range between 0.01 and 2.0 V.

Cathodic sweep in the first cycle of the Sn–rGO-650 shows two intense and broad peaks recorded at approximately 0.70 and 0.14 V, which are associated with the SnO_2 reduction and SEI formation (eqn (1)) and with the alloying process into Li_xSn (eqn (2)), respectively. Subsequent cycles (2nd, 3rd and 4th) recorded for this sample show four well defined peaks at 1.49, 0.88, 0.37 and 0.26 V. The peak observed at 0.88 V is associated with the reduction of SnO_2 to Sn, and those peaks recorded below 0.37 V can be attributed to the alloying process between Li and Sn to produce the Li_xSn alloy.[34] The peak that appeared at 1.49 V, which is only observed in the second cycle, could be ascribed to the electrolyte decomposition coupled with the irreversible reduction of functional groups still present on the graphene sheets.

The first anodic sweep of Sn–rGO-650 shows four peaks centered at 0.55, 0.65, 0.82 and 1.27 V. Those peaks observed at voltages under 0.90 V have been previously attributed to lithium dealloying from Li_xSn (eqn (2)), while the peak recorded at 1.27 V is due to the reversible redox reaction of Sn and SnO_2.[34] The anodic sweeps of the subsequent cycles are quite similar to the curve recorded for the first cycle, and only show small shifts compared to the pristine ones.

$$SnO_2 + 4Li^+ + 4e^- \rightarrow 2Li_2O + Sn \qquad (1)$$

$$Sn + xLi^+ + xe^- \leftrightarrow Li_xSn \ (0 \leq x \leq 4.4) \qquad (2)$$
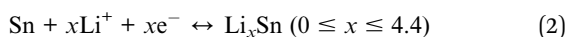
The CV curves recorded for sample Sn–rGO-800 (Fig. 4) show in the first cathodic sweep several broad peaks below 1.40 V that are associated, first, with the electrolyte decomposition, SEI formation and at lower voltage to the formation of the Li_xSn alloy. The anodic sweep of the first CV also exhibits very broad peaks at 0.46, 0.70 and 0.82 V attributed to the dealloying of Li_xSn to Sn. The second and subsequent cathodic sweeps are better defined than the first one, and three peaks centered at 0.36, 0.50 and 0.64 V are clearly observed. The peak detected at 0.36 V corresponds to the formation of the Li_xSn alloys, and the other two low intense peaks (0.50 and 0.64 V) are associated with the SEI formation.[32,35] In addition to these three peaks, another quite intense one at 1.45 V was also clearly observed in the second cycle curve that vanished in the following cycles. This later peak, which is more pronounced than the one observed in the case of the sample Sn–rGO-650, can be ascribed to the irreversible reduction of some species afforded from the electrolyte decomposition. The anodic sweeps of Sn–rGO-800 show four peaks at ca. 0.46, 0.63, 0.73 and 0.82 V, which have been previously assigned to the transition from the Li_xSn alloy to Sn.[35–38]

The galvanostatic charge–discharge curves recorded for the three samples (rGO, Sn–rGO-650 and Sn–rGO-800) in the first, second and fifth cycles measured at a current density of 50 mA g^{-1} in the potential window of 0.005–2.0 V vs. Li$^+$/Li are depicted in Fig. 5. Cyclic life and the evolution of the coulombic efficiency with charge–discharge cycles are also shown in Fig. 5. In all the cases, the specific capacity values were calculated based on the total mass of the electrodes and are summarised in Table 2 at different stages of the galvanostatic cycling.

The first cycle of the charging process recorded for the tin-free sample (rGO in Fig. 5) shows a very smooth profile with an associated specific capacity of 1154 mA h g^{-1}. This latter capacity value strongly decays to 515 mA h g^{-1} during the second charge, showing the irreversible processes that occur during the insertion/extraction of lithium ions such as SEI formation, but the subsequent reversible capacities were observed to be quite stable over the first 50 cycles and a capacity of 287 mA h g^{-1} has been observed at the end of the 50th cycle. The irreversible capacity afforded in the first cycle, which has
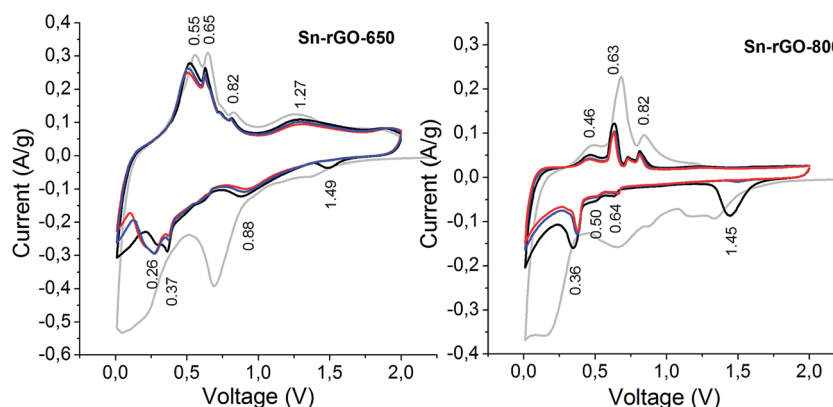

Fig. 4 First four cyclic voltammetry cycles recorded for the samples Sn−rGO-650 and Sn−rGO-800. First cycle (gray lines), second cycle (black lines), third cycle (blue lines) and fourth cycle (red lines).
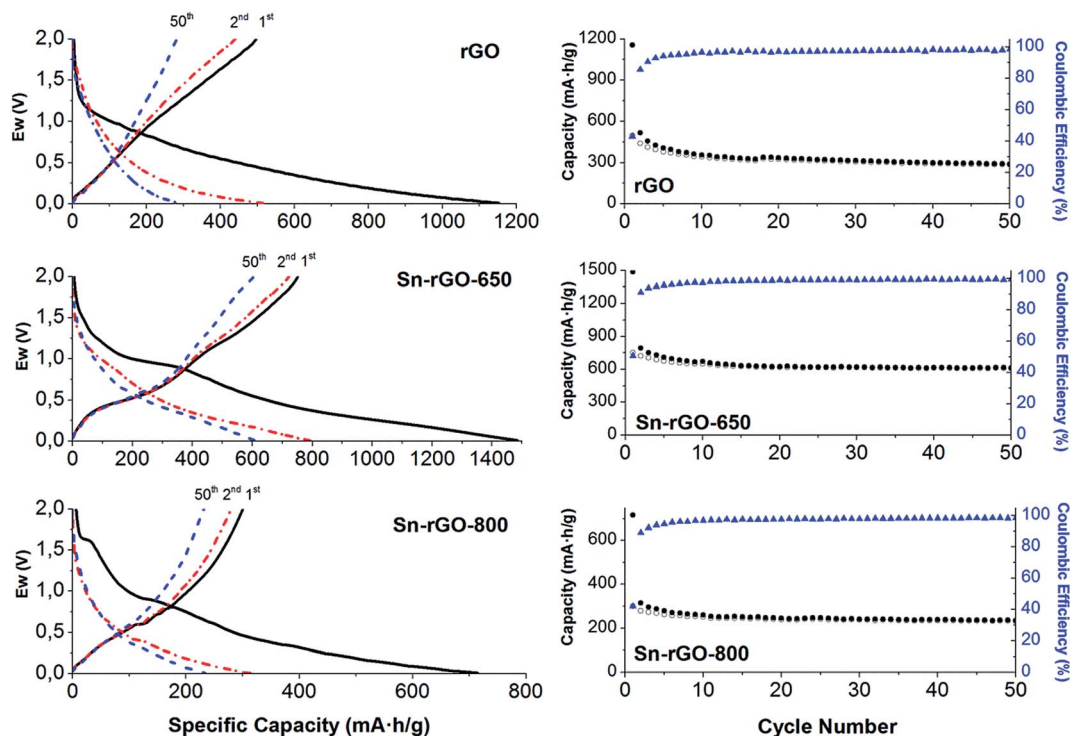
Fig. 5 First, second and fiftieth charge and discharge curves recorded for the labeled samples (left column). Specific capacities measured from the charge (filled circles) and discharge (empty circles) curves recorded at different cycles and their associated coulombic efficiencies (triangles) (right column).

been previously ascribed to the SEI formation, is amplified on materials with large specific surface areas.

Sn–rGO-650 exhibited a significant overall improvement in comparison with tin-free samples. The first charge curve showed a different profile compared with the curve obtained for the Sn-free sample. The first charge branch recorded for the Sn–rGO-650 sample shows a plateau around 1.0 V, not observed in the subsequent charge curves, which can be ascribed to the SEI formation. The specific capacity values obtained in this first cycle for the charge and discharge are 1481 and 755 mA h g^{-1}, respectively. Such large capacities are associated with the redox reaction of the SnO$_2$ along with the alloying/dealloying of the Sn nanoparticles that are formed during the reduction process in addition to the lithium insertion/extraction in the rGO. In the subsequent cycles (2nd to 50th), reversible specific capacities over 611 mA h g^{-1} were obtained.

The first charge curve of the Sn–rGO-800 (Fig. 5) also shows a large plateau around 1.0 V similar to the one observed for the Sn–rGO-650 and a specific capacity of 715 mA h g^{-1} was

measured in the former case. In this latter case, a plateau around 1.6 V is also observed during the first charge that could be attributed to the electrolyte decomposition. The second charge curve shows some steps at 0.8, 0.7 and 0.6 V that were maintained in the subsequent 30 cycles. These small plateaus are in good agreement with the results observed by cyclic voltammetry, and can be ascribed to the transition from the Li$_x$Sn alloy to metallic Sn. At a certain cycle (30th cycle) these steps vanish and are not further observed, suggesting that at this point Sn particles do not contribute anymore to the capacity. Similar behaviour has been previously reported by Lou *et al.*[39] in a system formed by 80 nm Sn particles coated with a carbonaceous shell which claimed that large Sn particles did not have enough space to accommodate volume changes making only possible their reaction at the outer parts of the spheres.

At this point we wondered what could be the reasons for the differences found in the electrochemical behaviour between the samples Sn–rGO-650 and Sn–rGO-800. In the literature, it has been previously claimed that small Sn-based nanoparticles can be beneficial to reach high specific capacity values and stability.[40] However, in the present case, both SnO$_2$ and Sn particles are quite large (~250 and ~700 nm, respectively) compared with most of the Sn-based particles studied as anodes for LIBs.

So, to obtain insight into the possible causes for the deactivation of the sample calcined at 800 °C, electrochemical impedance spectroscopy (EIS) measurements of the samples were performed after 50 cycles (Fig. 6). Nyquist plots of the three samples (Fig. 6A) exhibit a characteristic profile of these sorts of

Table 2 Specific capacity values (mA h g^{-1}) calculated from the charge sweep and their associated coulombic efficiencies (in brackets) measured at 50 mA g^{-1} for the samples at different cycles

	1st	2nd	50th
rGO	1154 (43%)	515 (85%)	287 (98%)
Sn–rGO-650	1481 (51%)	793 (91%)	611 (99%)
Sn–rGO-800	715 (42%)	314 (89%)	234 (98%)

This journal is © The Royal Society of Chemistry 2015

J. Mater. Chem. A, 2015, 3, 13402–13410 | 13407

composites, which includes a semicircle in the high-medium frequency range in combination with a straight line in the low frequency range.[41] The charge transfer resistance (R_{ct}) is quite similar in both Sn-containing samples (approximately 100 ohms) and a little bit higher than the R_{ct} measured for the rGO sample (33 ohms). As it can be observed, EIS curves corresponding to the Sn-containing samples did not show great differences between them and appeared almost overlapped, discarding a possible decomposition process that would lead to the deposition of an insulator layer, which is the main reason why these two samples behaved differently. To further characterise these samples, two coin cells already cycled for 50 cycles were opened and the electrode materials were checked on SEM (Fig. 6). The differences observed between both Sn-containing samples are quite clear. While SnO_2 particles were pulverized into very small nanoparticles produced during their reduction into metallic Sn, those particles that were initially present within the Sn–rGO-800 sample did not show any appreciable change regarding particle size and integrity, being well preserved after 50 charge discharge cycles, and only the formation of a shell around them is observed. It seems that the reaction in such big Sn particles could only proceed at the surface of the spheres or at the outer parts of the spheres avoiding their pulverization and significantly reducing the specific capacity measured on this sample.

To further evaluate the rate capability and stability of the sample Sn–rGO-650, a new fresh sample with 1.2 mg in mass, 12 mm in diameter and 0.07 mm in thickness (density ~ 0.15 g cm^{-3}) was prepared and its specific capacity was measured at different current rates (Fig. 7). The first charge capacity showed a value of 1550 mA h g^{-1} and the reversible capacity measured at 0.05 A g^{-1} is stabilized at 657 mA h g^{-1}. Measurements at 0.1, 0.2, 0.4, 0.6, 0.8 and 1 A g^{-1} showed highly stable capacity values of 627, 615, 566, 512, 440 and 415 mA h g^{-1}, respectively, with associated coulombic efficiencies over 98%. Once 80 cycles were completed within the voltage window (0.005–2.0 V), the cell was further charged-discharged within the range of 0.005 to 3.0 V to test the behaviour of the material in this voltage window (Fig. 7). Four different rates (0.05, 0.5, 1 and 2 A g^{-1}) were explored within this voltage window, and the capacity calculated at these rates showed average values of 940, 750, 660, and 470 mA h g^{-1}, respectively. Once 140 cycles were completed, the current rate was restored to 0.05 A g^{-1} showing improved values of specific capacities that reached values of 1010 mA h g^{-1} after 150 cycles, and further highlighting the good performance of this material as anodes for LIBs. In Table 3 are summarized some representative values recently reported for composites formed by graphene and SnO_2. It should be noted that in all these cases both the specific capacities and current rates are referred to the mass of the active material. It can be observed that when these values are recalculated to the mass of the whole electrode (see Table 3), the Sn–rGO-650 sample exhibits comparable or even better performance than composites that make use of conductive carbons to improve their electrical conductivities.

The cycling performance of this sample was further tested within the voltage window between 0.005 and 3.0 V at a current
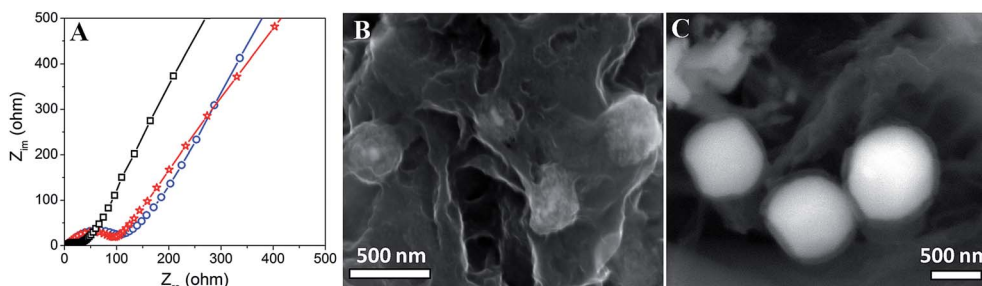

Fig. 6 EIS curves of rGO (squares), Sn–rGO-650 (stars) and Sn–rGO-800 (circles) recorded after 50 charge–discharge cycles, and SEM images of Sn–rGO-650 (B) and Sn–rGO-800 (C) samples after 50 charge–discharge cycles.
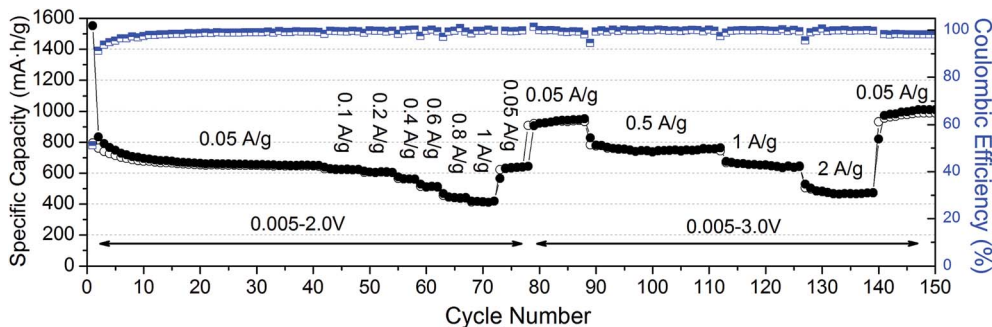

Fig. 7 Charge (filled circles) and discharge (empty circles) specific capacities and their associated coulombic efficiencies (bi-color squares) calculated for the Sn–rGO-650 sample along different cycles, measured at different current rates within the 0.005–2.0 V and 0.005–3.0 V voltage windows.

13408 | *J. Mater. Chem. A*, 2015, **3**, 13402–13410

This journal is © The Royal Society of Chemistry 2015

Table 3 Specific capacity values (mA h g^{-1}) measured at different current rates (A g^{-1}) calculated per mass of the active material and per mass of the electrode recently reported for systems based on SnO$_2$ and graphene composites

Reference	Formulation[a]	Capacity[b] (mA h g^{-1})	Current[b] (A g^{-1})	Capacity[c] (mA h g^{-1})	Current[c] (A g^{-1})
42	60 : 20 : 20	1100	0.072	660	0.043
		690	3.6	414	2.1
43	80 : 10 : 10	1359	0.1	1087	0.08
		1005	0.7	804	0.56
18	80 : 10 : 10	1123	0.3	898	0.2
		818	2.0	654	1.6
44	80 : 10 : 10	982	0.2	713	0.16
		536	1.6	429	1.3
22	80 : 10 : 10	1171	0.2	936	0.16
		700	2.0	560	1.6
45	70 : 10 : 20	878	0.1	610	0.07
		519	2.0	363	1.4
This work	100 : 0 : 0			1010	0.05
				750	0.5
				660	1.0

[a] Active material: conductive carbon: binder in wt% of the whole electrode. [b] Specific capacities and current rates measured per mass of the active material. [c] Specific capacities and current rates calculated per mass of the electrode.

rate of 2.0 A g^{-1}. It should be highlighted that after 400 cycles, namely more than 4 months under continuous charge–discharge stages (not shown), the electrode still delivers reversible specific capacities over 350 mA h g^{-1} and associated coulombic efficiencies over 98.5%, pointing out the stability of this composite and its good performance as anodes for LIBs.

Conclusions

Macroporous foams formed by the walls of reduced graphene oxide and SnO$_2$ submicron particles have been prepared by a very simple route, which involves the freeze/freeze drying of a GO suspension in the presence of tin sulphate and its subsequent pyrolysis at 650 °C under an inert atmosphere. These 3D monolithic structures can be easily compressed to obtain flexible films giving an additional value to the materials. The interpenetrated rGO layers arranged in a 3D macroporous structure afforded a suitable environment to accommodate the SnO$_2$ submicron particles providing good mechanical stability and electrical conductivity to the composite and allowing its use without the need for adding any conductive carbon. The performance of this material as binder-free anodes for LIBs showed high stability after 400 cycles and reversible capacities of 1010 and 470 mA h g^{-1} per mass of the electrode measured at 50 mA g^{-1} and 2 A g^{-1}, respectively.

SEM studies performed for this sample showed that the induced reaction of SnO$_2$ with Li upon voltage decrease causes the pulverization to very small SnO$_2$ particles, which remain highly active along cycling. An increase in the calcination temperature from 650 °C to 800 °C leads to the complete carbothermal reduction of the SnO$_2$ particles into metallic Sn with the particle size up to 700 nm. As a consequence of this particle growth, the specific capacity of this latter sample is much lower compared to the capacity exhibited by SnO$_2$-based samples and fades upon cycling mainly due to its large particle size. The complete deactivation of Sn particles occurred after 30 charge–discharge cycles, pointing out that in this particular case the particle size is determinant on its performance as anodes for LIBs. Further studies are under way to test these flexible 3D SnO$_2$–rGO composites in a full cell configuration.

Acknowledgements

References

1 J. M. Tarascon and M. Armand, *Nature*, 2001, **414**, 359.
2 N. Li, Z. Chen, W. Ren, F. Li and H.-M. Cheng, *Proc. Natl. Acad. Sci. U. S. A.*, 2012, **109**, 17360.
3 K. Rana, S. D. Kim and J.-H. Ahn, *Nanoscale*, 2015, **7**, 7065.
4 C. Wang, Y. Li, Y.-S. Chui, Q.-H. Wu, X. Chen and W. Zhang, *Nanoscale*, 2013, **5**, 10599.
5 Y. Idota, T. Kubota, A. Matsufuji, Y. Maekawa and T. Miyasaka, *Science*, 1997, **276**, 1395.
6 X. W. Lou, Y. Wang, C. Yuan, J. Y. Lee and L. A. Archer, *Adv. Mater.*, 2006, **18**, 2325.
7 P. Gurunathan, P. M. Ette and K. Ramesha, *ACS Appl. Mater. Interfaces*, 2014, **6**, 16556.
8 J. S. Chen and X. W. Lou, *Small*, 2013, **9**, 1877.
9 X. Zhou, W. Liu, X. Yu, Y. Liu, Y. Fang, S. Klankowski, Y. Yang, J. E. Brown and J. Li, *ACS Appl. Mater. Interfaces*, 2014, **6**, 7434.
10 J. Hassoun, G. Derrien, S. Panero and B. Scrosati, *Adv. Mater.*, 2008, **20**, 3169.
11 K. S. Novoselov, A. K. Geim, S. V. Morozov, D. Jiang, Y. Zhang, S. V. Dubonos, I. V. Grigorieva and A. A. Firsov, *Science*, 2004, **306**, 666.
12 J. Yao, X. Shen, B. Wang, H. Liu and G. Wang, *Electrochem. Commun.*, 2009, **11**, 1849.

13 L.-S. Zhang, L.-Y. Jiang, H.-J. Yan, W. D. Wang, W.-G. Song, Y.-G. Guo and L.-J. Wan, *J. Mater. Chem.*, 2010, **20**, 5462.

14 S.-M. Paek, E. J. Yoo and I. Honma, *Nano Lett.*, 2009, **9**, 72.

15 Y. Jiang, T. Yuan, W. Sun and M. Yan, *ACS Appl. Mater. Interfaces*, 2012, **4**, 6216.

16 S. H. Choi, J.-K. Lee and Y. C. Kang, *Nano Res.*, 2015, **8**, 1584.

17 S. Ding, D. Luan, F. Y. C. Boey, J. S. Chen and X. W. Lou, *Chem. Commun.*, 2011, **47**, 7155.

18 W. Zhou, J. Wang, F. Zhang, S. Liu, J. Wang, D. Yin and L. Wang, *Chem. Commun.*, 2015, **51**, 3660.

19 D. Cai, T. Yang, B. Liu, D. Wang, Y. Liu, L. Wang, Q. Lia and T. Wang, *J. Mater. Chem. A*, 2014, **2**, 13990.

20 D. Wang, J. Yang, X. Li, D. Geng, R. Li, M. Cai, T.-K. Sham and X. Sun, *Energy Environ. Sci.*, 2013, **6**, 2900.

21 B. Chen, H. Qian, J. Xu, L. Qin, Q.-H. Wu, M. Zheng and Q. Dong, *J. Mater. Chem. A*, 2014, **2**, 9345.

22 Y. Huang, D. Wu, J. Wang, S. Han, H. Lv, F. Zhang and X. Feng, *Small*, 2014, **10**, 2226.

23 X. Zhou, L.-J. Wan and Y.-G. Guo, *Adv. Mater.*, 2013, **25**, 2152.

24 Y. Huang, D. Wu, S. Han, S. Li, F. Zhang and X. Feng, *ChemSusChem*, 2013, **6**, 1510.

25 S. Nardecchia, D. Carriazo, M. L. Ferrer, M. C. Gutiérrez and F. del Monte, *Chem. Soc. Rev.*, 2013, **42**, 794.

26 B. Wang, W. Al Abdulla, D. Wang and X. S. Zhao, *Energy Environ. Sci.*, 2015, **8**, 869.

27 G. Zeng, N. Shi, M. Hess, X. Chen, W. Cheng, T. Fan and M. Niederberger, *ACS Nano*, 2015, **9**, 4227.

28 S. Han, J. Jiang, Y. Huang, Y. Tang, J. Cao, D. Wu and X. Feng, *Phys. Chem. Chem. Phys.*, 2015, **17**, 1580.

29 C. Botas, P. Álvarez, C. Blanco, R. Santamaría, M. Granda, P. Ares, F. Rodríguez-Reinoso and R. Menéndez, *Carbon*, 2012, **50**, 275.

30 D. Li, M. B. Müller, S. Gilje, R. B. Kaner and G. G. Wallace, *Nat. Nanotechnol.*, 2008, **3**, 101.

31 X. W. Lou, J. S. Chen, P. Chen and L. A. Archer, *Chem. Mater.*, 2009, **21**, 2868.

32 X. Zhou, J. Bao, Z. Dai and Y.-G. Guo, *J. Phys. Chem. C*, 2013, **117**, 25367.

33 X. Zhou, W. Liu, X. Yu, Y. Liu, Y. Fang, S. Klankowski, Y. Yang, J. E. Brown and J. Li, *ACS Appl. Mater. Interfaces*, 2014, **6**, 7434.

34 X.-T. Chen, K.-X. Wang, Y.-B. Zhai, H.-J. Zhang, X.-Y. Wu, X. Wei and J.-S. Chen, *Dalton Trans.*, 2014, 3137.

35 X. Zhou, L.-J. Wan and Y.-G. Guo, *Adv. Mater.*, 2013, **25**, 2152.

36 W.-M. Zhang, J.-S. Hu, Y.-G. Guo, S.-F. Zheng, L.-S. Zhong, W.-G. Song and L.-J. Wan, *Adv. Mater.*, 2008, **20**, 1160.

37 D. Deng and J. Y. Lee, *Angew. Chem., Int. Ed.*, 2009, **48**, 1660.

38 L. Ji, Z. Lin, B. Guo, A. J. Medford and X. Zhang, *Chem.–Eur. J.*, 2010, **16**, 11543.

39 X. W. Lou, J. S. Chen, P. Chen and L. A. Archer, *Chem. Mater.*, 2009, **21**, 2868.

40 P. G. Bruce, B. Scrosati and J.-M. Tarascon, *Angew. Chem., Int. Ed.*, 2008, **47**, 2930.

41 M. Ara, K. Wadumesthrige, T. Meng, S. O. Salley and K. Y. Simon Ng, *RSC Adv.*, 2014, **4**, 20540.

42 S. Nam, S. J. Yang, S. Lee, J. Kim, J. Kang, J. Y. Oh, C. R. Park, T. Moon, K. T. Lee and B. Park, *Carbon*, 2015, **85**, 289.

43 L. Liu, M. An, P. Yang and J. Zhang, *Sci. Rep.*, 2015, **5**, 9055.

44 S. Li, W. Xie, S. Wang, X. Jiang, S. Peng and D. He, *J. Mater. Chem. A*, 2014, **2**, 17139.

45 S. J. R. Prabakar, Y.-H. Hwang, E.-G. Bae, S. Shim, D. Kim, M. S. Lah, K.-S. Sohn and M. Pyo, *Adv. Mater.*, 2013, **25**, 3307.